Improving the mechanical properties of a sodium borosilicate glass through spinodal decomposition

Shi, Menghan; Sun, Daming; Christensen, Johan Frederik Schou; Jensen, Lars Rosgaard; Wang, Deyong; Smedskjær, Morten Mattrup

Published in:
Journal of the American Ceramic Society

DOI (link to publication from Publisher):
10.1111/jace.20099

Publication date:
2024

Document Version
Publisher's PDF, also known as Version of record

Received: 27 April 2024 | Revised: 12 July 2024 | Accepted: 29 July 2024

DOI: 10.1111/jace.20099

Journal of the American Ceramic Society

RESEARCH ARTICLE

Improving the mechanical properties of a sodium borosilicate glass through spinodal decomposition

Menghan Shi[1] | **Daming Sun**[1] | **Johan F. S. Christensen**[1] | **Lars R. Jensen**[2] | **Deyong Wang**[2] | **Morten M. Smedskjaer**[1]

[1]Department of Chemistry and Bioscience, Aalborg University, Aalborg, Denmark

[2]Department of Materials and Production, Aalborg University, Aalborg, Denmark

Correspondence
Morten M. Smedskjaer, Department of Chemistry and Bioscience, Aalborg University, Aalborg, 9220, Denmark.
Email: mos@bio.aau.dk

Funding information
China Scholarship Council, Grant/Award Numbers: 202207000028, 202107000016; HORIZON EUROPE European Research Council, Grant/Award Number: 101044664

Abstract

The brittleness of oxide glasses remains a critical problem, limiting their suitability for high-performance and safety-critical applications. In this study, we attempt to address this by synthesizing nanostructures in sodium borosilicate glasses through phase separation. While most previous work on the mechanical properties of phase-separated glasses has focused on phase separation through nucleation and growth, we here create interconnected structures through spinodal decomposition. Interestingly, this leads to improvements in Vickers hardness (from 5.8 to 6.2 GPa), crack initiation resistance (from 4.9 to 8.1 N), and fracture toughness (from 0.85 to 1.09 MPa·m$^{1/2}$). We show that the interconnected glassy phases deflect the propagating cracks, causing the required energy for cracks to cross phase boundaries to increase when subjected to external stress. This study deepens the understanding of how to address the brittleness problem of oxide glasses and provides a promising way to design high-performance glass materials.

KEYWORDS
crack resistance, fracture toughness, oxide glasses, phase separation

1 | INTRODUCTION

Glass materials continue to be used in various applications, such as architectural glasses, heat-resistant cookware, glassware in laboratories, and touchscreens, due to their properties of, for example, transparency, high hardness, and excellent chemical stability.[1,2] Among them, oxide glasses are the most widely used and constitute more than 95% of all commercial glass products.[3] However, the inherent brittleness of oxide glasses limits the scope of their applications, especially when subjected to high local tensile stress, which can lead to catastrophic failure and cause serious safety accidents.[4] It is therefore important to develop methods to improve the crack resistance (resistance to crack/flaw initiation) and fracture toughness (resistance to crack growth) of oxide glasses.

Crack resistance (CR) and fracture toughness (K_{Ic}) are key properties characterizing the fracture behavior of oxide glasses. CR describes the ability of oxide glasses to resist crack initiation upon sharp contact loading[5] while K_{Ic} is the critical value of the stress intensity factor for mode I fracture and describes the resistance of glasses to crack propagation.[6] Currently, various studies have attempted to explore crack initiation[7–9] and propagation

mechanisms.[10–13] The enhancement of *CR* is mainly achieved by rationally designing the glass composition, for instance, using topological engineering principles to regulate the glass composition[14] by increasing the Al_2O_3 content in binary aluminosilicate glasses[15] or increasing the fraction of trigonal boron in sodium borosilicate glasses.[16] Additionally, subjecting the glass to surface aging in a humid atmosphere has also proven to enhance CR.[17] The improvement of K_{Ic} can be achieved by altering external conditions such as residual compressive stress[18] and crack deflection,[19] but also by optimizing the internal atomic structure including changing the coordination number[20] and bonding energy of the atoms.[21] Previous work on compositional manipulation[16,22] or changing microstructures in glass ceramics[23,24] has shown that it is challenging to simultaneously increase CR and K_{Ic}.

Phase separation in glasses has been found to affect K_{Ic}, with observations of both increase and decrease in K_{Ic} compared with that of the corresponding homogeneous glasses.[4,23,24] Phase-separated glasses can, for example, be obtained by heat treatment,[25] electric field induction,[26] or remelting under steam pressure.[27] Phase-separated glass microstructures are formed either through "nucleation and growth" or spinodal decomposition.[28] Nucleation and growth occur in a metastable region of the phase diagram and result in a microstructure consisting of a matrix phase with randomly distributed distinct spherical droplet phases. Spinodal decomposition occurs in the unstable region, resulting in a microstructure of two phases interconnected with each other. Although there have been many studies on the microstructuring mechanism and mechanical properties of phase-separated glasses, they mainly focus on droplet-type phase separation (nucleation and growth).[29–32] As such, the effect of spinodal-type phase separation on the mechanical properties of glass is not yet fully understood.

Many studies have been carried out on the phase separation of sodium borosilicate (NBS) glasses. The homogeneous NBS glasses are widely used for their excellent optical properties, chemical durability, and thermal stability,[33,34] including the famous Pyrex glass.[35] Phase-separated NBS glasses are used industrially, including the Vycor process glass. Here, the phase-separated NBS glass is placed in an acid solution to leach out the sodium-borate-rich phase, thus obtaining a high-silica-rich phase.[35] Fundamental studies of phase separation in NBS glasses include Haller et al.[36] who studied NBS glasses with varying compositions and obtained a ternary phase diagram of the metastable immiscibility surface. Sander et al.[35] investigated the effect of long-term heat treatment on the phase separation of NBS glasses, evaluated the evolution of the microstructural parameters, such as pore size, and provided insight into the kinetics of microstructure formation. Aboutaleb et al.[37] found that phase separation in NBS glasses may weaken their chemical durability.

In this study, we have chosen an NBS glass to understand the effect of spinodal decomposition on mechanical properties.[36,38,39] Previously, Häßler et al.[29] studied a droplet-type phase-separated glass with a composition of 60 SiO_2–37 B_2O_3–3 Na_2O, finding that the four-point bending strength of the glass depends on the difference in thermal expansion coefficients of the droplet phase and the matrix phase. Seal et al.[23] evaluated the fracture toughness of NBS glass with spinodal-type phase separation using the Vickers indentation technique, finding that interconnecting phase separation increased the fracture toughness. However, additional work is needed given the inaccuracy of the Vickers indentation technique to determine fracture toughness,[40] and no details on CR were reported. Therefore, we select an appropriate glass composition (10.1 Na_2O–27.1 B_2O_3–62.8 SiO_2) that is known to give rise to spinodal-type phase separation during appropriate heat treatment.[36] We test the changes in glass microstructure, optical transparency, and mechanical properties, including both Vickers indentation and single-edge precracked beam fracture toughness tests.

2 | METHODS

2.1 | Sample preparation

We used a traditional melt-quenching method to synthesize a homogeneous NBS glass with the molar composition 10.1 Na_2O–27.1 B_2O_3–62.8 SiO_2. The mixture of powders [Na_2CO_3 (≥99.5%, Honeywell International), H_3BO_3 (≥99.5%, Sigma-Aldrich), and quartz (fine granular, 99.95%, Sigma-Aldrich)] was first added to a Pt-Rh crucible, followed by melting in an electric furnace at 1450°C for 1 h. Then, the melt was poured onto a brass plate and pressed with a plate of steel to ensure fast cooling. To improve the chemical homogeneity, the quenched glass was crushed and then remelted in the Pt-Rh crucible at 1450°C for 1 h. Finally, the melt was poured onto the brass plate for the second quench, and then quickly transferred to an annealing furnace preheated to the estimated glass transition temperature (500°C) for 30 min of annealing, and finally slowly cooled to room temperature.

The glass transition temperature of the homogeneous glass was found to be 510°C, as obtained by differential scanning calorimetry (DSC) (STA 449 F1, Netzsch). For this measurement, the sample was placed in a Pt crucible and heated to 680°C in an argon flow of 40 ml/min at a heating rate of 10°C/min. The DSC heating scans for all samples are shown in Figure S1, and the temperature

at the intersection between the tangent of the inflection point of the endothermic peak and the extrapolated heat flow of the glass was defined as the glass transition temperature.

To obtain the phase-separated glasses, we cut the homogeneous glass into small pieces and then heat-treated them. Based on the work of Haller et al.[36] and Seal et al.,[23] the heat treatment temperature was set to 650°C for durations of 8, 16, and 24 h, respectively. After the heat treatment, the samples were cooled to room temperature in the furnace at a rate of ~2 K/min. The as-prepared homogeneous glass is labeled as NBS-AP, while the phase-separated glasses are named NBS-8, NBS-16, and NBS-24 according to the duration of the heat treatment. All the glass samples were then cut into different sizes according to experimental requirements, and then first ground in ethanol using SiC grinding papers with gradually increasing grit size (from 220 to 4000 grit) before finally being polished with a 1-μm anhydrous diamond suspension.

2.2 | Structure characterization

X-ray diffraction (XRD) characterization (Empyrean XRD, PANalytical) was carried out to verify that the homogeneous and phase-separated glasses obtained after heat treatment are noncrystalline. The XRD measurements were performed using monochromatic Cu Kα radiation with a scanning angle from 5° to 75°, a voltage of 40 kV, and a scanning speed of 1.75°/min.

To determine the microscopic morphology of the samples, we performed field emission scanning electron microscopy (SEM) (Zeiss 1540XB) with an operating voltage of 10 kV. Before testing, we polished the samples and etched them in 10% HF for 7 s. This was done to remove the least durable phase through etching and thus enable visualization of the phase-separated microstructures, as has also been done in previous work.[32] After etching, the samples were coated with gold prior to measurement. SEM was also used to observe the crack paths in homogeneous and phase-separated glasses. That is, we observed corner cracks induced by Vickers indenter using a load of 9.8 N (see Section 2.5). These samples were not etched but coated with gold.

Micro-Raman spectroscopy (inVia, Renishaw) measurements were performed to characterize the structure of the glasses. A 532 nm laser was employed as the excitation source. We collected spectra in the wavenumber from 200 to 1400 cm^{-1} from three locations on each sample to ensure uniformity. Background correction and area normalization were systematically applied to all spectra.

2.3 | Optical transparency

To explore the effect of phase separation on optical transparency, we performed ultraviolet-visible (UV–vis) transmission spectroscopy (Cary 50 Bio, Varian) measurements. All samples were double-sided polished before spectral measurement. The samples were scanned in the wavelength range from 280 to 800 nm, with the scanning speed set to 60 nm/min. All UV–vis transmission spectra were normalized to a thickness of 1 mm.

2.4 | Elastic properties

We employed an ultrasonic thickness gauge (38 DL Plus, Olympus) to measure the elastic properties of the glasses, namely Young's modulus (E), Poisson's ratio (υ), shear modulus (G), and bulk modulus (B). All samples were cut into 1.2 × 1.2 × 0.3 cm^3, and both sides of the sample (1.2 × 1.2 cm^2) were polished. The thickness of the samples was input into the ultrasonic thickness gauge, and the transverse acoustic wave velocity (V_T) and longitudinal acoustic wave velocity (V_L) were measured using 20 MHz piezoelectric transducers. The elastic modulus could then be calculated using Equations (1)–(4)[41]:

$$E = \rho \frac{3V_L^2 - 4V_T^2}{\left(\frac{V_L}{V_T}\right)^2 - 1}, \tag{1}$$

$$\upsilon = \frac{V_L^2 - 2V_T^2}{2\left(V_L^2 - V_T^2\right)}, \tag{2}$$

$$G = \rho V_T^2, \tag{3}$$

$$B = \rho \frac{3V_L^2 - 4V_T^2}{3}, \tag{4}$$

where ρ is the density of the glass, which we determined by Archimedes' principle in ethanol.[42]

2.5 | Vickers indentation

Vickers hardness (H_V) and crack initiation resistance (CR) were determined through microindentation (CB500, Nanovea) with a Vickers indenter. To measure H_V, we pressed the indenter into the sample with a load of 2 N, employing a loading rate of 20 N/min, maintained the load for 15 s, and then gradually released the load with a rate of 20 N/min. The indent diagonal lengths of ten indentations for each sample were measured to determine the Vickers hardness. In these NBS glasses, cracks were found to occur

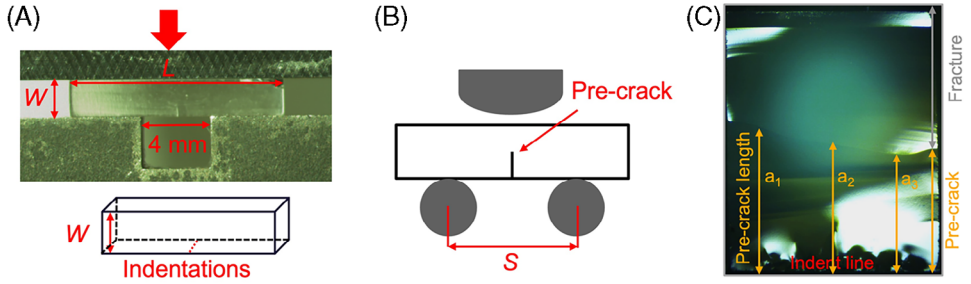

FIGURE 1 Fracture toughness measurement. (A) Image of precrack generation in the bridge-compression setup. (B) Schematic diagram of three-point bending method. (C) Image of postfractured SEPB specimen.

at the four indent corners at sufficiently high loads. By calculating the ratio of the number of corner cracks to the total number of corners, we obtained the crack probability. When the crack probability reaches 50%, the corresponding load is defined as the *CR* value.[43] To determine *CR* value using Vickers indentation, we subjected each sample to a set of different loads, from 2.0 to 9.8 N. The loading rate (N/min) was equal to ten times the indentation load (N), and this peak load was maintained for 15 s. We performed 30 indentations for each load. After the indentation experiment, the samples were placed in the laboratory air (temperature of 21°C, relative humidity of 30 ± 5 %) for 24 h before examining the indentations with optical microscopy.

2.6 | Single-edge precracked beam

We determined the fracture toughness (K_{Ic}) by the single-edge precracked beam (SEPB) method. The samples for SEPB measurements were rectangular cuboid-shaped with size of 1.5 × 2.0 × 10 mm^3, where B = 1.5 mm was the width of the narrow side, W = 2.0 mm was the width of the broad side, and L = 10 mm was the length.[5] The samples were polished, and a row of Vickers indents (8–10) was placed at the center of the narrow side of the sample with a load of 9.8 N (see the location of the indentation line in Figure 1A). Following the *CR* results, we found this load to be sufficient for producing corner cracks. The indents were placed in a row to ensure that the corner cracks produced by the indentations could connect, thereby forming a precrack in the next step. To this end, we used a universal testing machine (Z100, Zwick, with 1 kN load cell). The precrack was created by placing the sample as shown in Figure 1A, placing the narrow side with the indentations (B = 1.5 mm) over a groove of 4 mm width, with the indentations at the center of the groove (so-called bridge compression). Then, load was slowly applied from above at a loading rate of 0.05 mm/min. This allowed the precrack to grow on the broad side (W = 2.0 mm) in a controlled manner. We stopped applying load when the precrack had grown to the center of the broad side.

Then, the precracked sample was placed in the three-point bending fixture (Figure 1B), and a load was applied from above with a loading rate of 0.9 mm/min. Under load, the sample was completely fractured. The three-point bending span (S) was set to 8 mm, which met the span-to-width ratio of approximately 4 as required in the ASTM standard.[44] Figure 1C shows an image of the fractured surface, which was observed under an optical microscope. K_{Ic} could then be calculated using Equation (5)[45]:

$$K_{Ic} = \frac{P_{max}}{B\sqrt{W}} Y^*, \tag{5}$$

where P_{max} is the peak load, B is the width of the narrow side of the sample, W is the width of the broad side of the sample, and Y^* is the shape factor defined as

$$Y^* = \frac{3}{2}\frac{S}{W}\frac{\alpha^{1/2}}{(1-\alpha)^{3/2}} f(\alpha), \tag{6}$$

where S is the three-point bending span, α is the precrack length to width ratio ($\alpha = a/W$, where the precrack length is found as $a = [a_1+a_2+a_3]/3$, see Figure 1C), and $f(\alpha)$ is a function of α where $f(\alpha) = [1.99-(\alpha - \alpha^2)(2.15 - 3.93\alpha + 2.7\alpha^2)]/(1 + 2\alpha)$. The K_{Ic} result was obtained by averaging six valid tests for each glass sample.

3 | RESULTS

3.1 | Phase separation analysis

The XRD patterns shown in Figure S2 for both homogeneous and phase-separated glasses feature no sharp diffraction peaks, confirming that all samples are noncrystalline, also after being subjected to the heat treatment at 650°C which is above the glass transition temperature of 510°C for the homogeneous glass.

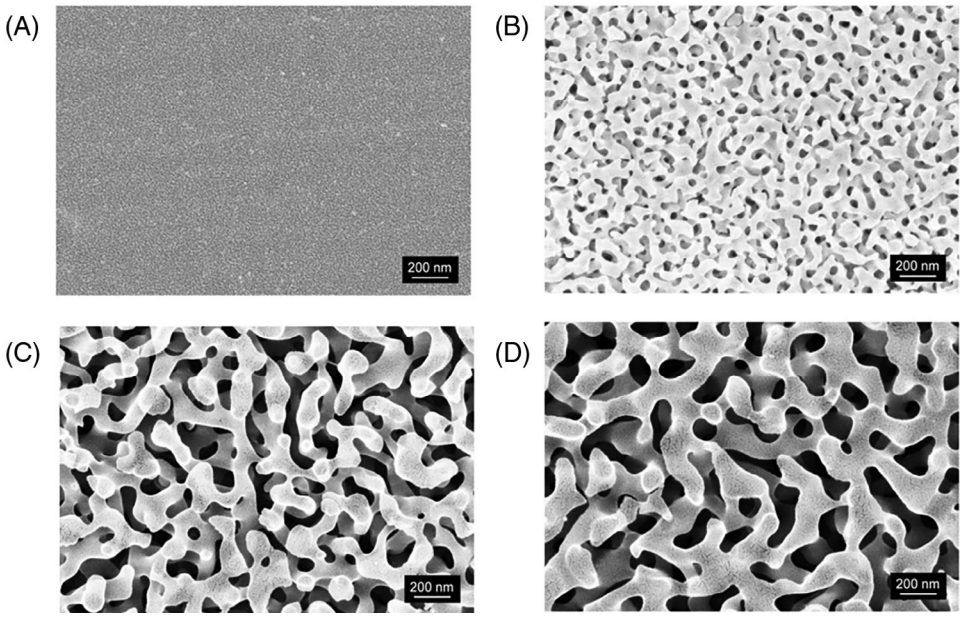

FIGURE 2 Scanning electron microscopy images of glass surface after etching with 10% HF: (A) NBS-AP, (B) NBS-8, (C) NBS-16, and (D) NBS-24.

The SEM images of the surface-etched glasses (Figure 2) show the microstructures formed by the heat treatment-induced phase separation. The observed microstructures are the glass phases that are not dissolved by the short-time etching in hydrofluoric acid. During the phase separation process, a boron-rich phase and a silicon-rich phase are formed according to the previous studies, and the hydrofluoric acid will mainly dissolve the boron-rich phase due to differences in chemical reactivity and solubility between the boron-rich and silicon-rich phases.[46,47] We note that the NBS-AP glass (Figure 2A) appears homogeneous, while networks of connected structures are observed in the NBS-8, NBS-16, and NBS-24 samples (Figures 2B–D). A longer heat treatment time is seen to make the structures larger and coarser. Interpenetrating structures are seen for all phase-separated samples, indicating that the induced phase separation occurs by spinodal decomposition (i.e., not by nucleation and growth), which is consistent with the study by Haller et al.,[36] In detail, according to this previous work, the molar compositions of the two observed phases in this work should be approximately 12 Na_2O–54 B_2O_3–34 SiO_2 (boron-rich phase) and 9 Na_2O–4 B_2O_3–87 SiO_2 (silicon-rich phase).

Figure 3A shows the Raman spectra of the homogeneous and phase-separated glasses. The band at 300 to 450 cm^{-1} reflects mixed bending and stretching modes of bridging Si-O-Si, Si-O-B, and/or B-O-B in the three-dimensional network.[48,49] The peak at 480 cm^{-1} (highlighted in Figure 3B) is due to Si-O-Si bending vibration and the breathing mode of the four-membered silicate ring.[50,51] As the heat treatment time increases, this peak moves slightly toward the lower wavenumber. There is a smaller peak at 800 cm^{-1} (highlighted in Figure 3C), which is ascribed to the stretching vibration of Si-O, primarily characterized by dominant Si motion,[52,53] and the signature downshifts to 770 cm^{-1} when a $BØ_3$ unit in the three-membered rings is replaced by a $[BØ_4]^{-1}$ unit.

The peaks at 770 and 800 cm^{-1} indicate the presence of B-O-B bonds rather than mixed Si-O-B bonds.[34] After heat treatment, the peak at 770 cm^{-1} is significantly enhanced, indicating an increase in the fraction of B-O-B bonds.[54] In addition, the band between 910–940 cm^{-1} may be caused by the fundamental breathing vibration of B-O stretching in the $[BØ_4]^{-1}$ unit and is also suspected to include Si-O-B_4 mixed bond stretching vibration modes.[55–57] The 1250–1550 cm^{-1} region is attributed to the trigonal $BØ_3$ structural unit.[58] Overall, we thus find relatively small changes in the Raman spectra with varying extent of phase separation. This is likely because, although we form a boron-rich and silicon-rich phase, there is no strong enthalpic preference for sodium cations to preferentially modify either the borate or silicate subnetworks.[59]

3.2 | Optical transmission properties

Figure 4A shows the optical images of the homogeneous and phase-separated samples of around 2.6 mm thickness after double-sided polishing. The homogeneous glass is clearly transparent and colorless, but as the heat treatment time increases, the opaqueness gradually increases and the transparency decreases. The UV–visible transmission

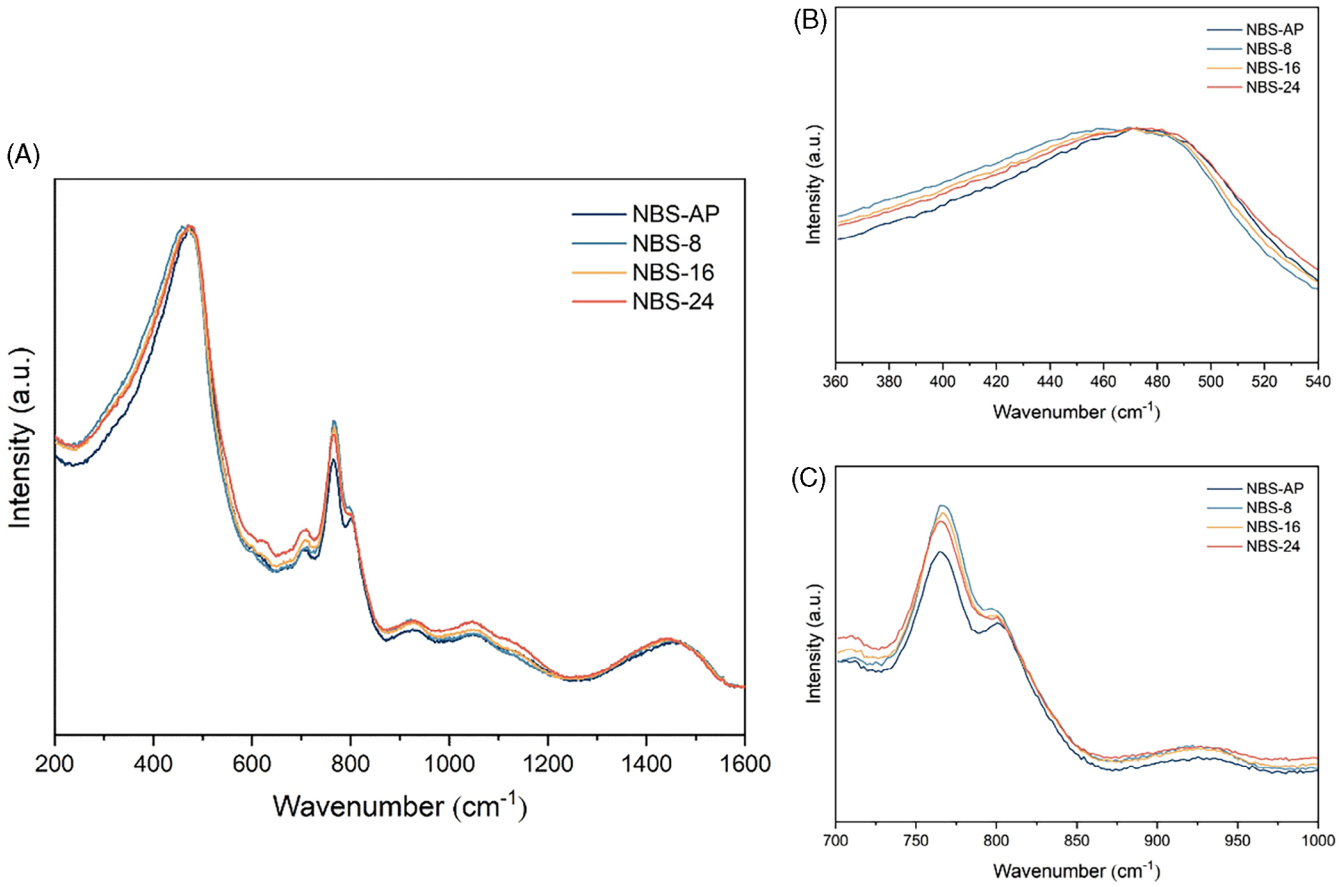

FIGURE 3 (A) Raman spectra of the homogeneous glass and the phase-separated glass samples heat-treated at 650°C for 8, 16, and 24 h. (B, C) Enlarged views of the Raman spectra in the (B) 360–540 cm^{-1} and (C) 700–1000 cm^{-1} regions.

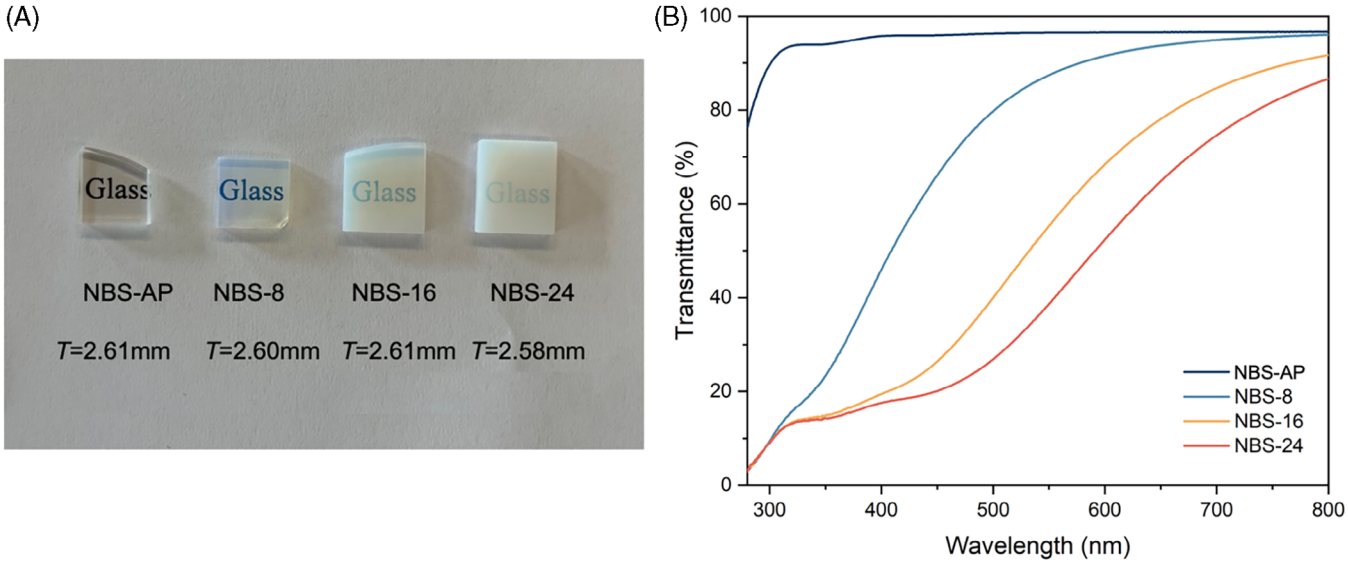

FIGURE 4 (A) Photographs of polished glasses before and after heat treatments, where *T* is the thickness of the sample. (B) UV–vis transmittance spectra of the as-prepared and heat-treated glasses.

TABLE 1 Mechanical properties of homogeneous and phase-separated glass samples. The numbers in parentheses represent standard deviations.

	NBS-AP	NBS-8	NBS-16	NBS-24
Density (g/cm^3)	2.294 (±0.001)	2.281 (±0.003)	2.287 (±0.002)	2.287 (±0.001)
Bulk modulus (GPa)	35.8 (±2.0)	35.0 (±0.8)	35.3 (±0.8)	35.6 (±0.6)
Shear modulus (GPa)	23.7 (±1.5)	23.6 (±0.6)	24.9 (±0.4)	24.9 (±0.5)
Young's modulus (GPa)	58.2 (±2.6)	57.7 (±1.0)	60.4 (±0.8)	60.6 (±1.0)
Poisson's ratio (−)	0.228	0.225	0.215	0.216
Hardness (GPa)	5.83 (±0.13)	5.97 (±0.12)	6.04 (±0.10)	6.16 (±0.10)
Crack resistance (N)	4.9	6.4	7.1	8.1
Fracture toughness (MPa·m$^{1/2}$)	0.85 (±0.09)	0.93 (±0.04)	0.96 (±0.18)	1.09 (±0.13)

spectra (Figure 4B) confirm that the transmittance of NBS-AP in the visible light range (400–800 nm) is above 95%, while increasing the heat treatment duration progressively reduces the transmittance in the visible range, especially in the low-wavelength region (blue light). The reduced transparency is caused by the light scattering occurring when the size of the microstructural features is similar to or larger than the wavelength of the light, thus the light scattering can be kept low when the microstructure is small in size.[60] As shown in Figure 4B, the transmittance of NBS-8 in the visible light range (400–800 nm) is markedly reduced compared with the NBS-AP in the low-wavelength range. As the phases formed by spinodal decomposition gradually grow in size with longer heat treatment time, the transmittances of the NBS-16 and NBS-24 samples are further reduced, also at higher wavelengths, but still most significantly at low wavelengths.

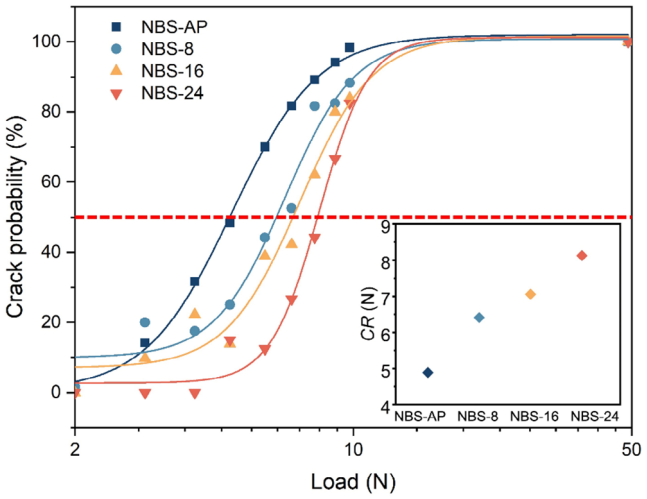

FIGURE 5 Crack probability as a function of applied indentation load for the glass samples. Inset: Crack resistance (*CR*) for the as-prepared and heat-treated glasses.

3.3 | Mechanical properties

Table 1 summarizes the mechanical properties of the glasses, including density, elastic moduli, Vickers hardness, crack initiation resistance, and fracture toughness. The density of the homogeneous glass is found to be 2.294 g/cm^3, and after heat treatment, it is between 2.281 and 2.287 g/cm^3, that is, the phase-separated glasses feature slightly more open volume. The ultrasound wavelengths in the elastic moduli measurements are significantly larger than the size of the separated phases, that is, the elastic moduli results reflect the joint influence of the two separated phases. The bulk modulus, shear modulus, and Young's modulus of NBS-8 therefore decrease only slightly compared with that of NBS-AP. The moduli of NBS-16 and NBS-24 then increase slightly compared with NBS-8. The Vickers hardness of the homogeneous glass is 5.83 GPa, which increases to 5.97, 6.04, and 6.16 GPa in the case of samples heat treated for 8, 16, and 24 h, respectively.

Figure 5 shows the crack occurrence probability curves of the homogeneous and heat-treated glasses. These curves are fitted with a sigmoidal function, $y = A_2 + (A_1 - A_2)/[1 + (x/x_0)^p]$, where A_1, A_2, x_0, and p are fitting constants.[10] The CR value is determined from this fitting curve as the load that corresponds to the crack probability of 50%. The determined CR values (inset in Figure 5) describe the glasses' resistance to crack initiation under contact loading. We find that the *CR* increases with the heat treatment time. That is, CR of the homogeneous glass is 4.89 N, while it increases to 6.41, 7.06, and 8.13 N upon heat treatments for 8, 16, and 24 h, respectively. Figure 6 shows the variation in fracture toughness of the samples. K_{Ic} of the homogeneous glass is 0.85 MPa·m$^{1/2}$, while it increases to 0.93, 0.96, and 1.09 MPa·m$^{1/2}$ upon heat treatments for 8, 16, and 24 h, respectively.

We next investigate how the microstructure affects the crack paths in the glasses by observing the path of cracks generated with Vickers indentation (Figure 7). The crack

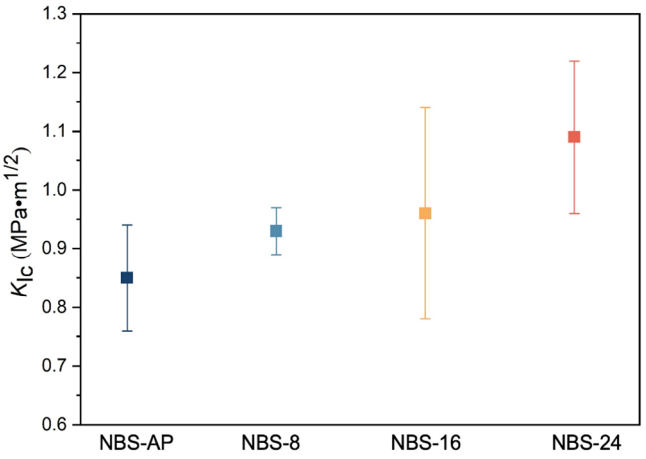

FIGURE 6 Fracture toughness (K_{Ic}) of the as-prepared and heat-treated samples determined using the single-edge precracked beam method. The error bars represent the standard deviations.

propagation path is very straight in the homogeneous glass shown in Figure 7A, while Figure 7B reveals how the crack is deflected due to the heterogeneous microstructure, being an obstacle for crack growth. This finding is consistent with previous work, showing that interconnected microstructures can influence the crack growth process.[61]

4 | DISCUSSION

Hardness, crack initiation resistance, and fracture toughness are found to be significantly improved by the induced phase separation with grid-like connections, while there is only a smaller effect on elastic properties. Thus, phase separation has a larger effect on local plastic deformation and cracking-related properties than elastic deformation occurring on scales larger than the microstructure. In the case of fracture toughness (related to crack growth resistance), the observed effect of phase separation agrees with some previous findings.[4,24] That is, when the crack needs to cross the phase boundary during its growth, crack arrest and/or crack deflection will hinder the propagation of the crack (Figure 7) as it requires greater energy to cross phase boundaries,[10,23] and thus the fracture toughness increases.

Previous research on the hardness of phase-separated glasses has mainly focused on droplet-type phase-separated glasses. Clark et al.[32] reported that the hardness of droplet-type phase-separated calcium aluminosilicate glasses is always lower than that of homogeneous glasses due to the weakest link principle. That is, when two glass phases are formed, one phase will be harder and one phase will be softer than the original glass. The softest phase is the weakest link and is more easily deformed, resulting in an overall reduction in hardness. At the same time, Clark et al.[32] also reported that the hardness of phase-separated glasses with acicular droplets is higher than that with spherical droplets. They explain this with a droplet-coalescence mechanism, where the acicular droplets deform and merge into fewer droplets of a lower surface-area-to-volume ratio during the indentation process. This process absorbs additional energy during yielding, resulting in higher hardness than for the glass with spherical droplets. Häßler et al.[29] studied the hardness of droplet-type phase-separated borosilicate glass (60 SiO_2–37 B_2O_3–3 Na_2O), observing reduced hardness upon phase separation. The stresses induced by phase separation were reported to increase the bending strength, as the difference in thermal expansion coefficient (CTE) of the phases leads to the droplets being under tension and the surrounding matrix being under radial tensile stress and tangential compressive stress. The tensile stresses might also be responsible for the reduced hardness upon phase separation, yet we note that the lower hardness is also in agreement with the above-mentioned weakest link principle. Xia et al.[62] studied spinodal-type phase-separated glasses and discovered that the hardness of aluminosilicate glasses increases upon phase separation. These authors proposed that according to the phase diagram, the volume proportion of the aluminum-rich phase (with a higher CTE) should be greater than that of the silicon-rich phase (with a smaller CTE), for example, the most abundant glass phase is under compressive stress, which could explain the increase in hardness. However, the impact of CTE difference between the phases in spinodal-type phase-separated glass on the resulting residual stresses is complex. For the present sodium borosilicate glass, Haller et al.[36] have reported that the volume ratio of the silicon-rich phase and the boron-rich phase after phase separation is around 50/50 upon heat treatment at 650°C. The boron-rich phase is found to be softer than the silicon-rich phase,[24] which could suggest reduced hardness upon phase separation according to the weakest link principle. However, we observe increased hardness for our spinodal-type phase-separated glasses (like Xia et al.[62]), indicating that the weakest link principle does not apply here. Unlike droplet-type phase separation, in spinodal-type phase separation, the two phases are interconnected, with the hard phase fixing the soft phase to prevent deformation, potentially explaining the higher hardness upon phase separation in the present glasses.

Considering crack initiation resistance, research by Zhang et al.[24] has demonstrated that heat treatment improves the crack resistance of droplet-type phase-separated glass (B_2O_3-SiO_2-Al_2O_3-P_2O_5). In the case of glass-ceramics, differences in CTE between droplet (crystal) and matrix (glass) will generate residual stresses during the heat treatment cooling process, which affects

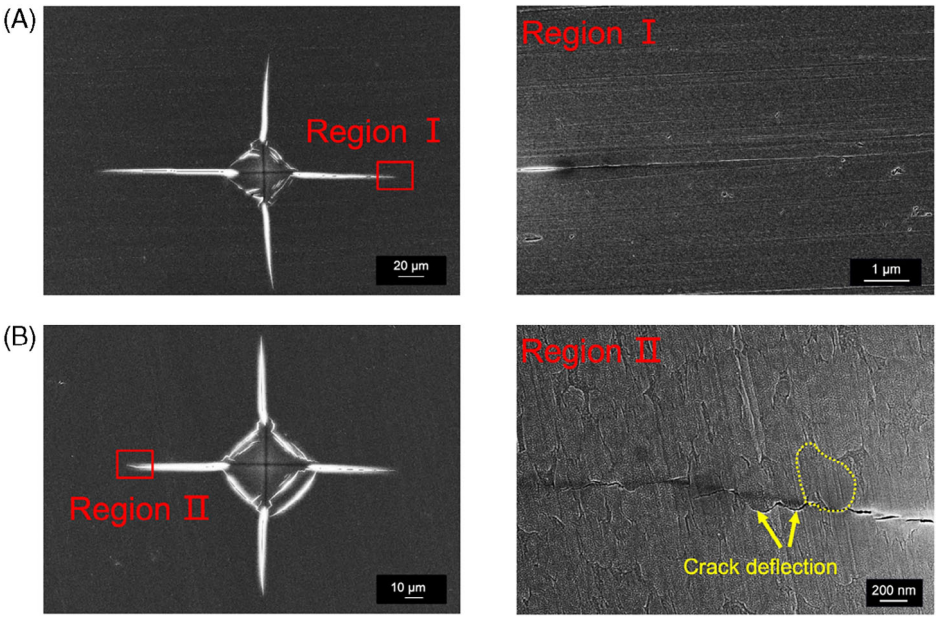

FIGURE 7 SEM images of the surface path of a radial crack formed by Vickers indentation (9.8 N) on (A) NBS-AP and (B) NBS-16 glass samples. The sample surfaces have been polished to an optical finish before indentation, but they have not been subjected to etching.

the crack resistance.[42] The study by Xia et al.[62] has also studied the effects of spinodal-type phase separation on crack resistance, finding that *CR* initially increases and then decreases as the heat treatment time increases, which is explained by two opposing effects. First, the interconnected phases form a barrier mechanism that increases the glass's resistance to crack initiation. Second, the mismatch in CTE between the two phases results in significant interfacial stress, promoting the occurrence of cracks. Santos et al.[63] have studied spinodal-type phase-separated $PbO–B_2O_3–Al_2O_3$ glasses and found that the mechanical properties are improved by the microstructure of the spinodal phase, including the high-volume fractions and extensive interconnection of the two phases, rather than residual stress.

In general, the highest CTE phase will be under tension, making it preferred for the crack to initiate and propagate through this phase. The effect this will have on the overall mechanical properties then depends on the properties of this phase. That is, it will be preferable to attract or arrest the cracks in the most ductile and tough phase. In the present work, we expect the boron-rich phase to have the highest CTE since high-SiO_2 content glasses generally feature low CTE.[64,65] At the same time, the softer boron-rich phase[24] generally features high CR due to its structural adaptability.[14] Overall, these effects should increase the phase-separated glass' ability to resist crack initiation and growth. However, we note that stress generation and interactions are complex in interconnected phases, and further experiments or simulations are needed to understand the role of the stiffness and toughness of the individual phases as well as the interface.

5 | CONCLUSION

In this work, we have obtained sodium borosilicate glasses with boron- and silicon-rich spinodal-type phase separation microstructures. The size of the structures formed by phase separation increases significantly with increasing heat treatment duration, which in turn affects the mechanical properties. While the density and elastic moduli are only slightly affected by the phase separation, we observe a significant improvement in the hardness, crack initiation resistance, and fracture toughness. The increase in hardness may be attributed to the formation of a harder phase that are controlling and hindering the deformation of the softer phase, as the phases are interconnected. The microstructure of spinodal-type phase separation is the primary factor in enhancing resistance to crack initiation and propagation. This is because the interconnected glass phases effectively hinder the propagation of cracks and form a barrier to resist crack initiation, causing the glass to require more energy to cross the phase boundary under external stress. Aggregation of the softer boron-rich phase, which is expected to attract cracks and have higher structural adaptability, lhelps to increase the resistance to crack initiation and growth. Finally, we note that while this study provides a method to simultaneously improve the crack resistance, fracture toughness, and hardness of borosilicate glass, it occurs at the expense of optical transparency, limiting any immediate application. In future studies, it will be interesting to explore if it is possible to tune the glass composition and heat treatment parameters to achieve a balance between toughening and transparency.

ACKNOWLEDGEMENTS

This work was funded by the China Scholarship Council (CSC nos. 202207000028, 202107000016) and the European Union (ERC, NewGLASS, 101044664). Views and opinions expressed are, however, those of the authors only and do not necessarily reflect those of the European Union or the European Research Council. Neither the European Union nor the granting authority can be held responsible for them.

CONFLICT OF INTEREST STATEMENT

The authors declare no conflict of interest.

ORCID

Johan F. S. Christensen https://orcid.org/0000-0002-8842-2843

Morten M. Smedskjaer https://orcid.org/0000-0003-0476-2021

REFERENCES

1. Mauro JC, Zanotto ED. Two centuries of glass research: historical trends, current status, and grand challenges for the future. Int J Appl Glass Sci. 2014;5:313–27.
2. Du T, Liu H, Tang L, Sørensen SS, Bauchy M, Smedskjaer MM. Predicting fracture propensity in amorphous alumina from its static structure using machine learning. ACS Nano. 2021;15(11):17705–16.
3. Varshneya AK, Mauro JC. Fundamentals of Inorganic Glasses. Elsevier; 2019.
4. Tang L, Krishnan NMA, Berjikian J, Rivera J, Smedskjaer MM, Mauro JC, et al. Effect of nanoscale phase separation on the fracture behavior of glasses: Toward tough, yet transparent glasses. Phys Rev Mater. 2018;2(11):113602.
5. To T, Sørensen SS, Christensen JFS, Christensen R, Jensen LR, Bockowski M, et al. Bond switching in densified oxide glass enables record-high fracture toughness. ACS Appl Mater Interfaces. 2021;13(15):17753–65.
6. Abdoli H, Alizadeh P, Boccaccini D, Agersted K. Fracture toughness of glass sealants for solid oxide fuel cell application. Mater Lett. 2014;115:75–78.
7. Cuadrado N, Casellas D, Anglada M, Jimenez-Pique E. Evaluation of fracture toughness of small volumes by means of cube-corner nanoindentation. Scr Mater. 2012;66:670–73.
8. Li X, Jiang L, Mohagheghian I, Dear JP, Li L, Yan Y. New insights into nanoindentation crack initiation in ion-exchanged sodium aluminosilicate glass. J Am Ceram Soc. 2018;101:2930–40.
9. Yang Y, Luo J, Huang L, Hu G, Vargheese KD, Shi Y, et al. Crack initiation in metallic glasses under nanoindentation. Acta Mater. 2016;115:413–22.
10. To T, Jensen LR, Smedskjaer MM. On the relation between fracture toughness and crack resistance in oxide glasses. J Non-Cryst Solids. 2020;534:119946.
11. Tandon R, Cook RE. Indentation crack initiation and propagation in tempered glass. J Am Ceram Soc. 1993;76:885–89.
12. Luo J, Deng B, Vargheese KD, Tandia A, DeMartino SE, Mauro JC. Atomic-scale modeling of crack branching in oxide glass. Acta Mater. 2021;216.
13. Wondraczek L, Dittmar A, Oelgardt C, Fabrice C, Ciccotti M, Christian M. Real-time observation of non-equilibrium liquid condensate confined at tensile crack tips in oxide glasses. J Am Ceram Soc. 2006;89:746–746.
14. Januchta K, Youngman RE, Goel A, Bauchy M, Logunov SL, Rzoska SJ, et al. Discovery of ultra-crack-resistant oxide glasses with adaptive networks. Chem Mater. 2017;29:5865–76.
15. Rosales-Sosa GA, Masuno A, Higo Y, Inoue H. Crack-resistant Al_2O_3–SiO_2 glasses. Sci Rep. 2016;6:23620.
16. Kato Y, Yamazaki H, Kubo Y, Yoshida S, Matsuoka J, Akai T. Effect of B_2O_3 content on crack initiation under vickers indentation test. J Ceram Soc Japan. 2010;118:792–98.
17. Liu P, Youngman RE, Jensen LR, Bockowski M, Smedskjaer MM. Achieving ultrahigh crack resistance in glass through humid aging. Phys Rev Materials. 2020;4:063606.
18. Wang Z, Guan T, Ren T, Wang H, Suo T, Li Y, et al. Effect of normal scratch load and hf etching on the mechanical behavior of annealed and chemically strengthened aluminosilicate glass. Ceram Int. 2020;46:4813–23.
19. Marco B. Toughening by Crack Deflection in the Homogenization of Brittle Composites with Soft Inclusions. Arch Ration Mech Anal. 2018;227:749–66.
20. Bauchy M, Wang B, Wang M, Yu Y, Qomi MJA, Smedskjaer MM, et al. Fracture toughness anomalies: viewpoint of topological constraint theory. Acta Mater. 2016;121:234–39.
21. To T, Sørensen SS, Christensen JFS, Christensen R, Jensen LR, Bockowski M, et al. Bond switching in densified oxide glass enables record-high fracture toughness. ACS Appl Mater Interfaces. 2021;13:17753–65.
22. Kato Y, Yamazaki H, Yoshida S, Matsuoka J. Effect of densification on crack initiation under Vickers indentation test. J Non-Cryst Solids. 2010;356:1768–73.
23. Seal AK, Chakraborti P, Roy NR, Mukherjee S, Mitra MK, Das GC. Effect of phase separation on the fracture toughness of SiO_2-B_2O_3-Na_2O glass. Bull Mat Sci. 2005;28(5):457–60.
24. Zhang Q, Jensen LR, Youngman RE, To T, Du T, Bauchy M, et al. Influence of phase separation microstructure on the mechanical properties of transparent modifier-free glasses. J Non-Cryst Solids. 2022;595:121806.
25. Onishchuk VI, Skuryatina EY, Zhernovaya NF, Marieva AV. Phase separation in borosilicate glasses synthesized in the material system soda-colemanite-quartz sand. Glass Ceram. 2020;76:323–27.
26. Liu W, Gu XM, Liang KM, Chen H, Zheng YK, Gu SR. Controlled phase separation by an electric field in glasses. Mat Sci Eng A. 1999;265:25–28.
27. Kreidl NJ, Maklad MS. Effect of water content on phase separation in soda-silica glasses. J Am Ceram Soc. 1969;52:508–9.
28. Shelby, JE. Introduction to glass science and technology. 2nd ed. Royal Society of Chemistry; 2005.
29. Häßler J, Rüssel C. Effect of microstructure of a phase separated sodium-borosilicate glass on mechanical properties. Ceram Int. 2017;43:11403–9.
30. Martel L, Allix M, Millot F, Sarou-Kanian V, Véron E, Ory S, et al. Controlling the size of nanodomains in calcium aluminosilicate glasses. J Phys Chem C. 2011;115(39):18935–45.
31. Miyata N, Jinno H. Strength and fracture surface energy of phase-separated glasses. J Mater Sci. 1981;16(8):2205–17.

32. Clark NL, Chuang S, Mauro JC. Mechanisms of microstructural deformation governing Vickers hardness in phase-separated calcium aluminosilicate glasses. J Am Ceram Soc. 2023;106:4605–16
33. Zhao Y, Zhang X, Yuan W, Liu F, Sun M, Peng H, et al. Composition effects on mechanical properties of pristine sodium borosilicate glass. Int J of Appl Glass Sci. 2019;10:363–70.
34. Tostanoski NJ, Möncke D, Youngman R, Sundaram SK. Structure-terahertz property relationship in sodium borosilicate glasses. Int J Appl Glass Sci. 2023;14:288–306.
35. Sander SAH, Weiss M, Denecke R, Enke D, Roggendorf H. Long-term heat treatment of phase separating sodium borosilicate glass. Adv Eng Mater. 2019;21:1900187.
36. Haller W, Blackburn DH, Wagstaff FE, Charles RJ. Metastable immiscibility surface in the system Na_2O-B_2O_3-SiO_2. J Am Ceram Soc. 1970;53:34–39.
37. Aboutaleb D, Douglad J, Safi B, Jbara O, Iratni A. Phase separation and chemical durability in the SiO_2-B_2O_3-Na_2O (SBN) glass system. Asian J Chem. 2012;24(2):473.
38. Ertuş EB, Vakifahmetoglu C, Öztürk A. Production and properties of phase separated porous glass. Ceram Int. 2020;46:4947–51.
39. Fritzsche JO, Rüdinger B, Deubener J. Slow coarsening of tetragonal zirconia nanocrystals in a phase-separated sodium borosilicate glass. J Non-Cryst Solids. 2023;606:122206.
40. Quinn GD, Bradt RC. On the Vickers indentation fracture toughness test. J Am Ceram Soc. 2007;90:673–80.
41. Poirier JP. Introduction to the physics of the earth's interior. Cambridge University Press; 2000.
42. Sun D, Zhang Q, Liu P, Jensen LR, Wang D, Smedskjaer MM. Balancing fracture toughness and transparency in barium titanosilicate glass-ceramics. Ceram Int. 2023;49:17479–87.
43. Frederiksen KF, Januchta K, Mascaraque N, Youngman RE, Bauchy M, Rzoska SJ, et al. Structural compromise between high hardness and crack resistance in aluminoborate glasses. J Phys Chem B. 2018, 122 6287–95.
44. C28 Committee. Standard Test Methods for Determination of Fracture Toughness of Advanced Ceramics at Ambient Temperature, ASTM International.
45. To T, Célarié F, Roux-Langlois C, Bazin A, Gueguen Y, Orain H, et al. Fracture toughness, fracture energy and slow crack growth of glass as investigated by the single-edge precracked beam (SEPB) and chevron-notched beam (CNB) methods. Acta Mater. 2018;146:1–11.
46. Scholes S, Wilkinson FCF. Glassy phase separation in sodium borosilicate glasses. Discuss Faraday Soc. 1970;50:175.
47. Hubert M, Faber AJ. On the structural role of boron in borosilicate glasses. Phys Chem Glasses. 2014;55:136–58.
48. Kwinda TI, Enke D, Koppka S. Effect of TiO_2 on microphase development during phase separation and crystallization in Na_2O–B_2O_3–SiO_2 glass system. J Am Ceram Soc. 2022;105:3261–78.
49. Manara D, Grandjean A, Neuville DR. Advances in understanding the structure of borosilicate glasses: a Raman spectroscopy study. Am Miner. 2009;94:777–84.
50. Ollier N, Boizot B, Reynard B, Ghaleb D, Petite G. β irradiation in borosilicate glasses: the role of the mixed alkali effect. Nucl Instr and Meth B. 2004;218:176–82.
51. Pasquarello A, Car R. Identification of raman defect lines as signatures of ring structures in vitreous silica. Phys Rev Lett. 1998;80:5145–47.
52. Ollier N, Gedeon O. Micro-Raman studies on 50 keV electron irradiated silicate glass. J Non-Cryst Solids. 2006;352(50–51):5337–43.
53. Boizot, B, Agnello, S, Reynard, B, Boscaino, R, Petite, G. Raman spectroscopy study of β-irradiated silica glass. J Non-Cryst Solids. 2003;325(1-3):22–28.
54. Chen D, Miyoshi H, Masui H, Akai T, Yazawa T. NMR study of structural changes of alkali borosilicate glasses with heat treatment. J Non-Cryst Solids. 2004;345–346:104–7.
55. Konijnendijk WL, Stevels J. The structure of borate glasses studied by Raman scattering. J Non-Cryst Solids. 1975;18(3):307–31.
56. Kamitsos E, Kapoutsis J, Jain H, Hsieh C. Vibrational study of the role of trivalent ions in sodium trisilicate glass. J Non-Cryst Solids. 1994;171(1):31–45.
57. Osipov A, Osipova L, Eremyashev V. Structure of alkali borosilicate glasses and melts according to Raman spectroscopy data. Glass Phys Chem. 2013;39(2):105–12.
58. Chen, LT, Ren, XT, Mao, YN, Mao, JJ, Zhang, XY, Wang, TT, et al. Radiation effects on structure and mechanical properties of borosilicate glasses. J Nucl Mater. 2021;552:153025.
59. Bødker MS, Sørensen SS, Mauro JC, Smedskjaer MM. Predicting composition-structure relations in alkali borosilicate glasses using statistical mechanics. Front Mater. 2019;6:175.
60. Beall GH, Duke DA. Transparent glass-ceramics. J Mater Sci. 1969;4:340–52
61. Simmons CJ, Freiman SW. Effects of phase separation on crack growth in borosilicate glass. J Non-Cryst Solids. 1980;38–39:503–8.
62. Xia F, Wang X, Wang Y, Ren X, Qiao A, Tao H. Tuning the hardness and crack resistance through liquid–liquid phase separation in an aluminosilicate glass. Phys Chem Chem Phys. 2023;25:17619–26.
63. Santos GG, Peitl O, Koike A, Akiba S, Sawamura S, Nagano M, et al. Residual stress versus microstructural effects on the strength and toughness of phase-separated PbO–B_2O_3–Al_2O_3 glasses. J Am Ceram Soc. 2022;106(1):596–612.
64. Cassar DR, Mastelini SM, Botari T, Alcobaça E, de Carvalho ACPLF, Zanotto ED, Predicting and interpreting oxide glass properties by machine learning using large datasets. Ceram Int. 2021;47(17):23958–72.
65. Ravinder R, Sridhara KH, Bishnoi S, Grover HS, Bauchy M, Jayadeva Kodamana H, et al. Deep learning aided rational design of oxide glasses. Mater Horiz. 2020;7(7):1819–27.

SUPPORTING INFORMATION

Additional supporting information can be found online in the Supporting Information section at the end of this article.

How to cite this article: Shi M, Sun D, Christensen JFS, Jensen LR, Wang D, Smedskjaer MM. Improving the mechanical properties of a sodium borosilicate glass through spinodal decomposition. J Am Ceram Soc. 2024;107:8367–77. https://doi.org/10.1111/jace.20099